



ALMA 26 arcmin² Survey of GOODS-S at One-millimeter (ASAGAO): X-Ray AGN Properties of Millimeter-selected Galaxies

Y. Ueda¹ , B. Hatsukade² , K. Kohno^{2,3} , Y. Yamaguchi² , Y. Tamura⁴, H. Umehata⁵ , M. Akiyama⁶ , Y. Ao⁷ ,
I. Aretxaga⁸ , K. Caputi⁹ , J. S. Dunlop¹⁰, D. Espada^{7,11} , S. Fujimoto¹² , N. H. Hayatsu¹³, M. Imanishi⁷ , A. K. Inoue¹⁴ ,
R. J. Ivison^{10,15} , T. Kodama⁶ , M. M. Lee^{7,16} , K. Matsuoka¹⁷, T. Miyaji¹⁸, K. Morokuma-Matsui¹⁹ , T. Nagao²⁰,
K. Nakanishi^{7,11} , K. Nyland²¹, K. Ohta¹ , M. Ouchi¹² , W. Rujopakarn^{22,23,24} , T. Saito²⁵, K. Takaki⁷ , I. Tanaka²⁶ ,
Y. Taniguchi⁵, T. Wang^{2,7} , W.-H. Wang²⁷, Y. Yoshimura¹⁶, and M. S. Yun²⁸

¹ Department of Astronomy, Kyoto University, Kyoto 606-8502, Japan

² Institute of Astronomy, The University of Tokyo, 2-21-1 Osawa, Mitaka, Tokyo 181-0015, Japan

³ Research Center for the Early Universe, The University of Tokyo, 7-3-1 Hongo, Bunkyo-ku, Tokyo 113-0033, Japan

⁴ Department of Physics, Nagoya University, Furo-cho, Chikusa-ku, Nagoya 464-8601, Japan

⁵ The Open University of Japan, 2-11, Wakaba, Mihama-ku, Chiba, Chiba 261-8586, Japan

⁶ Astronomical Institute, Tohoku University, 6-3 Aramaki, Aoba-ku, Sendai 980-8578, Japan

⁷ National Astronomical Observatory of Japan, 2-21-1 Osawa, Mitaka, Tokyo 181-8588, Japan

⁸ Instituto Nacional de Astrofísica, Óptica y Electrónica (INAOE), Aptdo. Postal 51 y 216, 72000 Puebla, Pue., Mexico

⁹ Kapteyn Astronomical Institute, University of Groningen, 9700 AV Groningen, The Netherlands

¹⁰ Institute for Astronomy, University of Edinburgh, Royal Observatory, Blackford Hill, Edinburgh EH9 3HJ, UK

¹¹ The Graduate University for Advanced Studies (SOKENDAI), 2-21-1 Osawa, Mitaka, Tokyo, 181-8588, Japan

¹² Institute for Cosmic Ray Research, The University of Tokyo, Kashiwa, Chiba 277-8582, Japan

¹³ Department of Physics, The University of Tokyo, 7-3-1 Hongo, Bunkyo-ku, Tokyo 113-0033, Japan

¹⁴ Department of Environmental Science and Technology, Faculty of Design Technology, Osaka Sangyo University, 3-1-1, Nakagaito, Daito, Osaka 574-8530, Japan

¹⁵ European Southern Observatory, Karl-Schwarzschild-Str. 2, D-85748 Garching, Germany

¹⁶ Department of Astronomy, The University of Tokyo, 7-3-1 Hongo, Bunkyo-ku, Tokyo 113-0033, Japan

¹⁷ Dipartimento di Fisica e Astronomia, Università di Firenze Via G. Sansone 1, I-50019 Sesto Fiorentino (Firenze), Italy

¹⁸ Instituto de Astronomía, Universidad Nacional Autónoma de México, Ensenada, Baja California, Mexico; P.O. Box 439027, San Diego, CA 92143-9027, USA

¹⁹ Institute of Space and Astronautical Science, Japan Aerospace Exploration Agency, 3-1-1 Yoshinodai, Chuo-ku, Sagami-hara, Kanagawa 252-5210, Japan

²⁰ Research Center for Space and Cosmic Evolution, Ehime University, 2-5 Bunkyo-cho, Matsuyama, Ehime 790-8577, Japan

²¹ National Radio Astronomy Observatory, 520 Edgemont Road, Charlottesville, VA 22903, USA

²² Department of Physics, Faculty of Science, Chulalongkorn University, 254 Phayathai Road, Pathumwan, Bangkok 10330, Thailand

²³ National Astronomical Research Institute of Thailand (Public Organization), Donkaew, Maerim, Chiangmai 50180, Thailand

²⁴ Kavli Institute for the Physics and Mathematics of the universe (WPI), The University of Tokyo Institutes for Advanced Study,

The University of Tokyo, Kashiwa, Chiba 277-8583, Japan

²⁵ Nishi-Harima Astronomical Observatory, Centre of Astronomy, University of Hyogo, 407-2 Nishigaichi, Sayo, Sayo-gun, 679-5313 Hyogo, Japan

²⁶ Subaru Telescope, National Astronomical Observatory of Japan, Japan

²⁷ Institute of Astronomy and Astrophysics, Academia Sinica, Taipei 10617, Taiwan

²⁸ Department of Astronomy, University of Massachusetts, Amherst, MA 01003, USA

Received 2017 July 29; revised 2017 November 26; accepted 2017 December 2; published 2018 January 18

Abstract

We investigate the X-ray active galactic nucleus (AGN) properties of millimeter galaxies in the Great Observatories Origins Deep Survey South (GOODS-S) field detected with the Atacama Large Millimeter/submillimeter Array (ALMA), by utilizing the *Chandra* 7-Ms data, the deepest X-ray survey to date. Our millimeter galaxy sample comes from the ASAGAO survey covering 26 arcmin² (12 sources at a 1.2 mm flux-density limit of ≈ 0.6 mJy), supplemented by the deeper but narrower 1.3 mm survey of a part of the ASAGAO field by Dunlop et al. Of the 25 total millimeter galaxies, 14 have *Chandra* counterparts. The observed AGN fractions at $z = 1.5\text{--}3$ are found to be $90_{-19}^{+8}\%$ and $57_{-25}^{+23}\%$ for the ultra-luminous and luminous infrared galaxies with $\log L_{\text{IR}}/L_{\odot} = 12\text{--}12.8$ and $\log L_{\text{IR}}/L_{\odot} = 11.5\text{--}12$, respectively. The majority ($\sim 2/3$) of the ALMA and/or Herschel detected X-ray AGNs at $z = 1.5\text{--}3$ appear to be star-formation-dominant populations, having $L_{\text{X}}/L_{\text{IR}}$ ratios smaller than the “simultaneous evolution” value expected from the local black-hole-mass-to-stellar-mass ($M_{\text{BH}}\text{--}M_{\star}$) relation. On the basis of the L_{X} and stellar mass relation, we infer that a large fraction of star-forming galaxies at $z = 1.5\text{--}3$ have black hole masses that are smaller than those expected from the local $M_{\text{BH}}\text{--}M_{\star}$ relation. This contrasts previous reports on luminous AGNs at the same redshifts detected in wider and shallower surveys, which are subject to selection biases against lower luminosity AGNs. Our results are consistent with an evolutionary scenario in which star formation occurs first, and an AGN-dominant phase follows later, in objects that finally evolve into galaxies with classical bulges.

Key words: galaxies: active – galaxies: high-redshift – galaxies: starburst – X-rays: galaxies

1. Introduction

A key issue in cosmic evolution is the growth history of supermassive black holes (SMBHs) in galactic centers and their stellar populations, leading to the tight bulge-mass-to-SMBH-mass correlation observed in the present universe (see

Kormendy & Ho 2013 for a recent review; following them, we use the term “bulge” only for classical bulges and elliptical galaxies). Overall good agreement between the star formation and mass-accretion history from $z \sim 3$ to $z \sim 0$ (e.g., Boyle & Terlevich 1998; Marconi et al. 2004; Aird et al. 2015; Ueda

2015) implies that they seem to have mostly “co-evolved” on cosmological timescales. It is not yet clear, however, how strictly stars and the SMBH were coeval in an individual galaxy. Large dispersion in the bulge-to-SMBH-mass ratio in high-redshift objects suggests that the evolution processes are more complex than a simple “co-evolution” hypothesis and that the observational result may be largely subject to the selection biases of the sample studied (Kormendy & Ho 2013).

Both star formation and mass-accretion comoving densities peak at $z \sim 2$ (Madau & Dickinson 2014; Ueda et al. 2014), which is often referred to as “cosmic noon.” Submillimeter observations discovered IR luminous galaxies (submillimeter galaxies; SMGs) at these redshifts, where violent star formation deeply enshrouded by dust takes place (e.g., Smail et al. 1997). These objects would be a key population for understanding the origin of galaxy-SMBH co-evolution; many theoretical studies suggest that major mergers trigger both star formation and mass accretion, making them appear as IR luminous galaxies containing an obscured AGN (e.g., Hopkins et al. 2006). Sensitive X-ray observations provide an efficient way to detect such AGNs (e.g., Alexander et al. 2005). Due to the limited angular resolution of previous (single-dish) sub/millimeter or FIR observatories ($10''$ – $20''$), however, it is often difficult to robustly determine their multiwavelength counterparts and thereby estimate their star formation rate and mass-accretion rate.

The Atacama Large Millimeter/submillimeter Array (ALMA) is changing the situation thanks to its unprecedented angular resolution and sensitivity at sub/millimeter wavelengths. The GOODS-S region is one of the best fields for studying faint AGNs in distant galaxies, because the deepest X-ray survey to date was performed with the *Chandra* observatory there (Luo et al. 2017). On the basis of an ALMA follow-up of SMGs in the Extended-*Chandra* Deep Field South (E-CDFS) field (ALMA LABOCA E-CDFS Submillimeter Survey, ALESS; Hodge et al. 2013), Wang et al. (2013) determined the AGN fraction to be $15^{+15}_6\%$ at an X-ray flux limit of 2.7×10^{-16} erg cm $^{-2}$ s $^{-1}$ (0.5–8 keV); hereafter, we refer to these AGNs as the “ALESS-AGN sample.” More recently, utilizing the *Chandra* 4 Ms and Karl G. Jansky Very Large Array (JVLA) survey catalogs, Rujopakarn et al. (2016) have identified 6 AGNs from 16 millimeter galaxies in the GOODS-S/ultra deep field (UDF) detected by Dunlop et al. (2017) (hereafter D17), two of which were first discovered in the ALMA spectroscopic survey covering a 1 arcmin 2 area in the UDF (ASPECS, Aravena et al. 2016). Using ALMA in cycle 3, our team has performed an unbiased deep 1.2 mm imaging survey over a 26 arcmin 2 region inside the GOODS-S-JVLA field (Alma twenty-Six Arcmin 2 survey of Goods-south At One-millimeter, ASAGAO), which fully encompasses the GOODS-S/UDF. This survey fills the gap in the survey parameter space (sensitivity and area) between the ALESS and the UDF survey. The results using the JVLA radio-continuum data, which are also important for identifying AGNs, will be reported in a separate paper (W. Rujopakarn et al. 2017, in preparation).

In this paper, we investigate the X-ray AGN properties of millimeter galaxies detected in our survey and that by D17, utilizing the latest *Chandra* 7 Ms source catalog (Luo et al. 2017). We mainly refer to the FourStar Galaxy Evolution Survey (ZFOURGE) catalog for identification of ALMA sources detected in the ASAGAO (the source catalog will be presented in B. Hatsukade et al. 2017, in preparation). The

ZFOURGE catalog also provides a sample of galaxies not detected with ALMA that are located in our survey region. We investigate relations among the X-ray luminosity (or mass-accretion rate), infrared luminosity (or star formation rate, SFR), and stellar mass of these samples, and discuss the implications on the galaxy-SMBH co-evolution at cosmic noon. Throughout the paper, we adopt the conversion from IR luminosity (without AGN contribution) to SFR as $\text{SFR}/(M_{\odot} \text{ yr}^{-1}) = 1.09 \times 10^{-10} L_{\text{IR}}/L_{\odot}$, which is based on the work of Kennicutt (1998) and recalibrated for a Chabrier (2003) initial mass function (IMF).²⁹ The cosmological parameters of $H_0 = 70$ km s $^{-1}$ Mpc $^{-1}$, $\Omega_M = 0.3$, and $\Omega_{\Lambda} = 0.7$ are adopted. The errors in the number fraction based on a small-size sample (≤ 10) are given at 1σ confidence limits referring to Table 6 of Gehrels (1986).

2. Millimeter Galaxy Catalog

2.1. Observations and Source Detection

ALMA band 6 (1.2 mm) observations of the $5' \times 5'$ (≈ 26 arcmin 2) area of the ASAGAO were conducted in 2016 September in the C40-6 array configuration for a total observing time of 45 hr (Project code: 2015.1.00098.S, PI: K. Kohno). The details of the observations and data reduction are described in B. Hatsukade et al. (2017, in preparation), and here we briefly summarize them. Two frequency tunings were adopted centered at 1.14 and 1.18 mm to cover a wider frequency range, whose central wavelength was 1.16 mm. The correlator was used in the time domain mode with a bandwidth of 2000 MHz (15.625 MHz \times 128 channels). Four basebands were used for each tuning, and the total bandwidth was 16 GHz, covering the 244–248 GHz, 253–257 GHz, 259–263 GHz, and 268–272 GHz frequency ranges. The number of available antennas was 38–45.

The data were reduced with Common Astronomy Software Applications (CASA; McMullin et al. 2007). The maps were processed with the CLEAN algorithm with the task `tclean`.³⁰ Clean boxes were placed when a component with a peak signal-to-noise ratio (S/N) above 5.0 is identified, and CLEANed down to a 2σ level. The observations were done with a higher angular resolution ($\sim 0''.2$) than originally requested ($0''.8$), and we adopted a *uv*-taper of 160 k λ to improve the surface brightness sensitivity, which gives a final synthesized beamsize of $0''.94 \times 0''.67$ and a typical rms noise level of 89 $\mu\text{Jy beam}^{-1}$.

Source detection was conducted on the image before correcting for the primary beam attenuation. The source and noise properties were estimated with the AEGEAN (Hancock et al. 2012) source-finding algorithm. We find 12 sources with a peak S/N threshold of 5.0σ , whereas no negative source with a peak S/N $< -5.0\sigma$ is found. The integrated flux density is calculated with elliptical Gaussian fitting. Table 1 (2–4th columns) lists the position of the peak intensity and the integrated flux density corrected for the primary beam attenuation with its 1σ error.

²⁹ Any SFR values quoted from the literature are re-scaled to this calibration.

³⁰ The adopted parameters are as follows: natural weighting, cell size of 0.15 arcsec, gridding of mosaic, specmode of multi-frequency synthesis, and nterms of 2.

Table 1
Millimeter and X-Ray Properties of ALMA Sources in GOODS-S

ID	R.A.	Decl.	$S_{1.2\text{ mm}}$	$S_{1.3\text{ mm}}$	$S_{1.2\text{ mm}}$	$\log L_{\text{IR}}$	$\log M_*$	CID	$S_X/10^{-17}$ (erg cm^{-2} s^{-1})	$\log N_{\text{H}}$	Γ	$\log L_X$	z	AGN Flag
(1)	(h m s)	(d m s)	(mJy)	(mJy)	(mJy)	(L_{\odot})	(M_{\odot})	(9)	(10)	(cm^{-2})	(12)	(erg s^{-1})	(14)	(15)
1	03:32:28.51	-27:46:58.37	2.58 ± 0.17	12.76 ± 0.01	10.8	522	4.7	$20.0^{+4.0}_{-0.0}$	$1.92^{+0.00}_{-0.02}$	$42.3^{+0.7}_{-0.2}$	2.38	NNYN
2	03:32:35.72	-27:49:16.26	2.16 ± 0.15	$12.83^{+0.04}_{-0.01}$	11.1	666	39.0	$23.6^{+0.1}_{-0.2}$	1.9	43.5 ± 0.1	2.582	YYYY
3 (=UDF1)	03:32:44.04	-27:46:35.90	1.53 ± 0.18	0.92 ± 0.08	...	12.75 ± 0.01	10.7 ± 0.10	805	107.0	20.0	$2.09^{+0.11}_{-0.11}$	44.0 ± 0.1	3.00	NYYY
4	03:32:47.59	-27:44:52.39	1.10 ± 0.15	12.61 ± 0.01	10.7	852	8.1	22 (fixed)	1.9	42.3 ± 0.2	1.94	NNYN
5	03:32:32.90	-27:45:40.95	1.40 ± 0.19	11.00 ± 0.01	10.3	...	<6.9	23 (fixed)	1.9	<41.5	0.523	...
6 (=UDF2)	03:32:43.53	-27:46:39.27	1.44 ± 0.22	1.00 ± 0.09	...	$12.50^{+0.06}_{-0.01}$	11.1 ± 0.15	...	<7.5	23 (fixed)	1.9	<42.8	2.92	...
7	03:32:29.25	-27:45:09.94	0.89 ± 0.17	$12.18^{+0.06}_{-0.01}$	10.5	538	10.5	$24.0^{+0.0}_{-0.6}$	1.9	$42.9^{+0.2}_{-0.4}$	2.01	YYNN
8 (=UDF3)	03:32:38.55	-27:46:34.52	0.72 ± 0.14	0.86 ± 0.08	0.553 ± 0.014	12.75 ± 0.01	10.3 ± 0.15	718	4.5	$20.0^{+3.6}_{-0.0}$	$2.44^{+0.00}_{-0.54}$	42.6 ± 0.2	2.62	NYYN
9	03:32:36.75	-27:48:03.81	1.05 ± 0.25	<2.3
10	03:32:44.60	-27:48:36.18	0.62 ± 0.14	11.97 ± 0.01	10.6	818	145.0	$23.1^{+0.1}_{-0.1}$	1.9	43.9 ± 0.1	2.593	NYYY
11	03:32:49.45	-27:49:09.21	1.34 ± 0.31	<5.7
12	03:32:31.47	-27:46:23.38	1.11 ± 0.28	12.42 ± 0.01	11.2	587	26.3	$23.3^{+0.2}_{-0.2}$	1.9	43.1 ± 0.1	2.225	YYYY
UDF4	03:32:41.01	-27:46:31.58	...	0.30 ± 0.05	...	11.92 ± 0.02	10.5 ± 0.15	...	<4.6	23 (fixed)	1.9	<42.5	2.43	...
UDF5	03:32:36.95	-27:47:27.13	...	0.31 ± 0.05	...	11.95 ± 0.03	10.4 ± 0.15	...	<3.9	23 (fixed)	1.9	<42.2	1.759	...
UDF6	03:32:34.43	-27:46:59.77	...	0.24 ± 0.05	...	11.88 ± 0.06	10.5 ± 0.10	...	<5.1	23 (fixed)	1.9	<42.1	1.411	...
UDF7	03:32:43.32	-27:46:46.91	...	0.23 ± 0.05	...	11.69 ± 0.18	10.6 ± 0.10	797	6.6	$20.0^{+4.0}_{-0.0}$	1.9	$42.4^{+0.7}_{-0.2}$	2.59	NNYN
UDF8	03:32:39.74	-27:46:11.63	...	0.21 ± 0.05	0.223 ± 0.022	12.12 ± 0.27	11.2 ± 0.15	748	284.0	$22.6^{+0.1}_{-0.1}$	1.9	43.7 ± 0.1	1.552	NYYY
UDF9	03:32:43.42	-27:46:34.46	...	0.20 ± 0.04	...	11.31 ± 0.48	10.0 ± 0.10	799	4.2	22 (fixed)	1.9	41.0 ± 0.2	0.667	NNNN
UDF10	03:32:40.75	-27:47:49.09	...	0.18 ± 0.05	...	11.60 ± 0.22	10.2 ± 0.15	756	2.5	$20.0^{+3.0}_{-0.0}$	$3.00^{+0.00}_{-1.10}$	42.4 ± 0.2	2.086	NNYN
UDF11	03:32:40.06	-27:47:55.82	...	0.19 ± 0.05	...	12.15 ± 0.26	10.8 ± 0.10	751	9.3	$21.8^{+1.0}_{-1.9}$	$1.90^{+0.42}_{-0.00}$	$42.4^{+0.2}_{-0.1}$	1.996	NNYN
UDF12	03:32:41.28	-27:47:42.61	...	0.15 ± 0.04	...	11.51 ± 0.17	9.6 ± 0.15	...	<2.0	23 (fixed)	1.9	<42.7	5.000	...
UDF13	03:32:35.09	-27:46:47.78	...	0.17 ± 0.04	...	11.78 ± 0.12	10.8 ± 0.10	655	4.7	$20.0^{+3.8}_{-0.0}$	$2.07^{+0.00}_{-0.17}$	$42.4^{+0.5}_{-0.2}$	2.497	NNYN
UDF14	03:32:40.96	-27:46:55.34	...	0.16 ± 0.04	...	11.59 ± 0.17	9.7 ± 0.10	...	<3.3	23 (fixed)	1.9	<41.5	0.769	...
UDF15	03:32:35.75	-27:46:54.98	...	0.17 ± 0.05	...	11.52 ± 0.31	9.9 ± 0.15	...	<1.8	23 (fixed)	1.9	<41.8	1.721	...
UDF16	03:32:42.37	-27:47:07.79	...	0.15 ± 0.04	...	11.55 ± 0.20	10.9 ± 0.10	...	<4.0	23 (fixed)	1.9	<42.0	1.314	...

Note. (1) ALMA source ID (those with “UDF” correspond to the D17 sources); (2) & (3) ALMA source position (J2000); (4) ALMA-integrated flux-density and 1σ error at 1.2 mm derived from the ASAGAO survey; (5) those at 1.3 mm derived from the UDF survey (D17); (6) those at 1.2 mm derived from the ASPECS (Aravena et al. 2016); (7) infrared luminosity in the rest 8–1000 μm band in units of solar luminosity (taken from D17 for the UDF sample and based on our SED fit for the ASAGAO sample) and its 1σ error; (8) stellar mass in units of solar mass (taken from D17 for the UDF sample and IDs 3, 6, and 8, and from Straatman (2016) for the rest); (9) *Chandra* source ID in Luo et al. (2017); (10) observed X-ray flux (or 90% confidence upper limit) in the 0.5–7 keV band converted from a count rate in the 0.5–7, 0.5–2, or 2–7 keV band with the apparent photon index Γ_{eff} ; (11) X-ray absorption hydrogen column density; (12) intrinsic photon index; (13) absorption-corrected X-ray luminosity (or 90% confidence upper limit) in the rest-frame 0.5–8 keV band; (14) adopted redshift (after Straatman 2016 or D17; three decimal digits is for spectroscopic redshifts and two is for photometric redshifts); (15) AGN flags for the criteria I through IV.

2.2. Definition of Our ALMA Sample

To supplement our ASAGAO sample, we also include fainter flux ALMA sources detected in the deep 1.3 mm image of the UDF ($\simeq 4.5$ arcmin² located inside the ASAGAO field) by D17. By position-matching ($< 0''.2$) and flux comparison, we find that the objects with IDs 3, 6, and 8 are identical to UDF1, UDF2, and UDF3 in D17, respectively. Table 1 (5th column) lists the 1.3 mm flux density of the D17 sources. We refer to D17 for the positions of these sources except UDF1, UDF2, and UDF3 (second and third columns of Table 1). In addition, we find that ID 8 (UDF3) and UDF8 are also detected in the 1.2 mm continuum map of the ASPECS (Aravena et al. 2016). The 1.2 mm fluxes obtained by ASPECS are listed in the 6th column of Table 1 for these sources. The fluxes of UDF3 obtained from ASAGAO and ASPECS are consistent within the errors.

The ASAGAO sources are cross-matched against the ZFOURGE catalog (Straatman 2016), after correcting for systematic astrometric offsets ($-0''.09$ in R.A. and $+0''.28$ in decl.) with respect to the ALMA image, which are calibrated by the positions of stars in the *Gaia* Data Release 1 catalog (Gaia Collaboration 2016) within the ASAGAO field. The ZFOURGE fully covers the ASAGAO 26 arcmin² field, in which ~ 3000 objects are cataloged with limiting magnitudes of K_S (AB) = 26.0–26.3 (5σ) at the 80% and 50% completeness levels with masking, respectively. We search for counterparts from the ZFOURGE catalog whose angular separation from the ALMA position is smaller than $0''.2$, corresponding to $\sim 3\sigma$ of the statistical positional error of ALMA for a point-like source; when a counterpart is largely extended (IDs 3 and 5), we allow a larger positional offset, up to 1 arcsec. Consequently, ZFOURGE counterparts are found for 10 sources, except for IDs 9 and 11. Since the chance probability that an unrelated object falls within a radius of $0''.2$ is only ≈ 0.004 as calculated from the source density of the ZFOURGE catalog, we can safely assume that all of these ALMA-ZFOURGE associations are true.³¹ We adopt the best-estimated redshift (spectroscopic or photometric) in the ZFOURGE catalog but refer to D17 for the UDF sample and IDs 3, 6, and 8. The adopted redshift is listed in the 14th column of Table 1. The differences between the photometric redshifts in the ZFOURGE catalog and the spectroscopic redshifts in D17 are found to be $\Delta z / (1 + z) < 0.08$ with a median of 0.02. This indicates that the photometric redshift errors minimally affect our analysis and conclusions.

We regard the 23 sources with ZFOURGE counterparts (10 sources from the ASAGAO excluding IDs 9 and 11, and 13 sources from D17 excluding the overlapping sources UDF1, UDF2, and UDF3; hereafter the ASAGAO sample and the UDF sample, respectively) as the parent sample for our subsequent studies. All of them are also detected in FIR bands (70–160 μm) with *Herschel*/PACS (Elbaz et al. 2011).

2.3. SED Fitting and Infrared Luminosities

To estimate the infrared luminosities (and hence SFRs) of the ASAGAO sample, we analyze their spectral energy distributions (SEDs), utilizing the MAGPHYS code (da Cunha et al. 2008, 2015). We use 43 optical-to-millimeter photometric data, including the ALMA, ZFOURGE, and de-blended *Herschel*/SPIRE photometries (T. Wang et al. 2017, in

preparation). Checking the ALMA spectra, we have confirmed that line contamination to the 1.2 mm continuum flux is ignorable in all the targets. We use the MAGPHYS high- z excitation code for the sources at $z > 1$, whereas the MAGPHYS original package is applied for ID 5 ($z = 0.523$). In the SED fitting, the redshift is fixed to the value in Table 1. The resultant infrared luminosities in the rest-frame 8–1000 μm band (L_{IR})³² are listed in the seventh column of Table 1. Further details on the SED analysis are given in Y. Yamaguchi et al. (2017, in preparation).

The infrared luminosities of the ASAGAO sample that we derive with the MAGPHYS code are found to be consistent with the L_{IR} values in D17 (for IDs 3, 6, and 8) and in Straatman (2016) within 0.1–0.2 dex in most cases; a maximum difference of ≈ 0.5 dex is found for ID 8 (UDF3) between our result and D17, whose 1.3 mm flux density was corrected for unusually large line emission in the analysis of D17. Straatman (2016) obtained the infrared luminosities by fitting the 24, 100, and 160 μm photometry with the Wuyts et al. (2008) template. For the UDF sample we refer to D17 for L_{IR} ,³³ these values were obtained by a SED fit to 24 μm to 1.3 mm photometry with the spectral template by Kirkpatrick et al. (2015). The listed L_{IR} values include an estimated 20% AGN contribution.

The flux densities of the ASAGAO sample range from ~ 0.6 to ~ 3 mJy. It bridges the ALESS sample (Hodge et al. 2013)³⁴ and the UDF sample (D17), which contain brighter and fainter sub/millimeter galaxies than the ASAGAO sources, respectively. The majority of our sources with ZFOURGE counterparts are located at $z \simeq 2 - 3$. No object at $z > 3$ has been identified, although it is possible that the two sources (IDs 9 and 11) lacking redshift constraints are $z > 3$ galaxies. This result is consistent with the findings by Aravena et al. (2016) and D17 that high- z galaxies are rare in the faint ALMA populations, as expected on the basis of the selection wavelength and depth of the survey (B  thermin et al. 2015). Of the 10 identified ASAGAO sources, 8 have infrared luminosities larger than $10^{12} L_{\odot}$ and hence are classified as ‘‘ultra-luminous infrared galaxies’’ (ULIRGs). The star formation rate (SFR) estimated from the infrared luminosity after subtracting an estimated 20% AGN contribution (D17) ranges 9–600 $M_{\odot} \text{ yr}^{-1}$.

3. Cross-matching with the *Chandra* 7 Ms Catalog

We cross-match the ALMA source list with the *Chandra* 7 Ms source catalog of the CDFS (Luo et al. 2017), which contains 1008 objects detected in 0.5–2 keV, 2–7 keV, and/or 0.5–7 keV bands, among which 137 objects are located within the ASAGAO field. The sensitivity limit of the *Chandra* data is $(2 - 8) \times 10^{-17} \text{ erg cm}^{-2} \text{ s}^{-1}$ (0.5–7 keV) for a power-law photon index of 1.4, which is not uniform in our ALMA

³¹ Some ZFOURGE objects may be lensing galaxies.

³² The MAGPHYS code returns the 3–1000 μm luminosities but we adopt these values as the conventional 8–1000 μm band luminosities for the ASAGAO sample because the contribution of the 3–8 μm band to total dust emission is negligible (Clemens et al. 2013).

³³ Following the recipe in Section 6.3 of D17, we converted the SFR_{FIR1} values in their Table 4 into L_{IR} using the Murphy et al. (2011) relation with a minor correction from a Chabrier to a Kruopa IMF.

³⁴ By transforming the 850 μm flux densities to the 1.2 mm ones, the ALESS fluxes reach a similar depth (~ 1 mJy) to that of the ASAGAO survey. The major difference is that the ALESS is pointed toward bright SMGs, while the ASAGAO is a blind survey.

survey region. A flux of 2×10^{-17} erg cm $^{-2}$ s $^{-1}$ (0.5–7 keV) corresponds to an intrinsic 0.5–8 keV luminosity of $\log L_X / (\text{erg s}^{-1}) = 41.7$ and 41.9 for a source at $z=2$ with an absorption of $\log N_H / \text{cm}^{-2} = 20$ and 23, respectively, assuming our model spectrum with a photon index of 1.9 (see below). X-ray counterparts are selected if the angular separation between the ALMA and *Chandra* sources is smaller than 3 times their combined 1σ positional error, which is dominated by the *Chandra* one (0.14–0.62 arcsec, depending on the photon counts). We found 14 X-ray counterparts to the 23 ALMA sources, 8 from the ASAGAO sample (10 objects), and 6 from the UDF sample (13 objects). We confirm that all 6 of the X-ray sources in the D17 sample reported by Rujopakarn et al. (2016) using the shallower *Chandra* 4 Ms catalog (Xue et al. 2011) are included. The probability of spurious identification is negligibly small, <0.01 , and is estimated from the surface number density of the *Chandra* sources in our ALMA survey region ($\sim 2 \times 10^4$ deg $^{-2}$).

Following the recipe described in Ueda et al. (2003), we estimate the column density and intrinsic (de-absorbed) luminosity of each *Chandra* object. As the model spectrum, we assume a cutoff power-law spectrum plus its reflection component from optically thick cold matter with a solid angle of 2π . Both the cutoff power law and its reflection are subject to intrinsic absorption at the source redshift and Galactic absorption, which is fixed at $N_H = 8.8 \times 10^{19}$ cm $^{-2}$. Such a reflection component from the torus and/or the accretion disk is known to be commonly present in the X-ray spectra of AGNs (e.g., Kawamuro et al. 2016). From the hardness ratio of the vignetting-corrected count rates in the 0.5–2 keV and 2–7 keV band, we first determine the apparent photon index by assuming no intrinsic absorption. If it is found to be larger than 1.9, then we adopt this value and consider no absorption. Otherwise, we fix the intrinsic photon index to 1.9 and determine the absorption to account for the observed hardness ratio. For objects detected only in the total (0.5–7 keV) band, we assume a photon index of 1.9 and an absorption column density of $\log N_H / \text{cm}^{-2} = 20$. Then, the intrinsic luminosity is calculated based on the photon index and normalization. The statistical error in the hardness ratio is taken into account to estimate the uncertainties in the photon index, absorption, and intrinsic luminosity. The results are listed in the 11–13th columns of Table 1.

The X-ray detection rate of our ALMA sample is $61\% \pm 10\%$ (14 out of 23), and for the ASAGAO sample it is $80_{-20}^{+13}\%$ (8 out of 10). We adopt criteria similar to those proposed by Wang et al. (2013) to classify an X-ray-detected object as an AGN: (I) the effective photon index (Γ_{eff}) is smaller than 1.0, suggestive of intrinsic absorption; (II) the de-absorbed rest-frame 0.5–8 keV luminosity (L_X) is larger than 3×10^{42} erg s $^{-1}$; (III) the apparent rest-frame 0.5–8 keV luminosity (L_X^{app}) is higher than 5 times that of the star formation ($L_{X, \text{SF}}$) estimated from the infrared luminosity according to the formula of Lehmer et al. (2010);³⁵ and (IV) the observed X-ray to MIR flux ratio is $\log(f_X / f_{3.6 \mu\text{m}}) > -1$. We then regard sources that satisfy at least one criterion (the 15th column of Table 1) and have $\log L_X > 41.5$ are AGNs. The 13 ALMA-*Chandra* objects, except UDF9, are classified as AGNs.

For the 9 ALMA sources that are not detected with *Chandra*, in Table 1 (10th and 13th columns) we list a 90% confidence upper limit for the observed flux (converted from the count-rate upper limit in that position by assuming a photon index of 1.4, that of the X-ray background, with no absorption), and that of the intrinsic luminosity obtained by assuming a photon index of 1.9 and an absorption of $\log N_H / \text{cm}^{-2} = 23$ as a typical spectrum for an obscured AGN when the redshift is known. We also perform a stacking analysis of the 7 Ms *Chandra* images for these 9 sources with the CSTACK program,³⁶ which utilizes event files reprocessed by Cappelluti et al. (2016) and Williams et al. (2017). No significant signals are detected in the 0.5–2 keV and 2–8 keV bands with 90% upper limits of 5×10^{-18} erg cm $^{-2}$ s $^{-1}$ and 2×10^{-17} erg cm $^{-2}$ s $^{-1}$ for the mean fluxes, respectively (assuming a photon index of 1.4).

To investigate the nature of the X-ray sources in the ASAGAO field that are not detected with ALMA, we cross-match them with the ZFOURGE catalog in the same way as above. We find that out of the 123 ALMA-undetected *Chandra* sources, 111 have ZFOURGE counterparts, among which 95 are detected *Herschel*/PACS and hence have estimates of their infrared luminosities. When we limit the redshift range to $z = 1.5$ –3, where most of the ALMA-*Chandra* sources reside, there are 49 *Chandra* sources within the ASAGAO field, out of which 46 have ZFOURGE counterparts. Among them, 13 are detected with ALMA (and also with *Herschel*), 26 with *Herschel* only, and 7 are neither detected with ALMA nor with *Herschel*. For comparison with our ASAGAO and UDF sample, we refer to the *Chandra* AGNs detected by *Herschel* but undetected by ALMA at $z = 1.5$ –3 as the “*Herschel*-AGN sample” in the subsequent discussions.

4. Results and Discussion

4.1. Correlation between Star Formation Rate and Stellar Mass

Figures 1 and 2 plot the relation between infrared luminosity and redshift and that between stellar mass (M_*) and SFR, respectively, for the X-ray sources in the ASAGAO and UDF samples (red circles and triangles), the ALESS-AGN sample (magenta squares), and the *Herschel*-AGN sample (black diamonds). We refer to Wang et al. (2013) and Straatman (2016) for the infrared luminosities of the ALESS-AGN and *Herschel*-AGN samples, respectively. For all the samples, we estimate the SFRs from L_{IR} after subtracting an assumed 20% AGN contribution. The stellar masses (listed in the 8th column in Table 1) are taken from the ZFOURGE catalog (Straatman 2016) for the ASAGAO (except IDs 3, 6, and 8) and *Herschel*-AGN samples, from D17 for the UDF sample and IDs 3, 6, and 8, and from Wang et al. (2013) for the ALESS-AGN sample (recalibrated for a Chabrier IMF). All the M_* values were derived with multiwavelength SED analyses by assuming the solar abundances, and represent the total stellar masses in the galaxies. In the figure, we draw the “main sequence” lines at $z = 2.75$, $z = 2.25$, and $z = 1.75$ according to Speagle et al. (2014). Figure 1 indicates that most of the ALMA-*Chandra* AGNs belong to main-sequence star-forming galaxies (SFGs), although a few ASAGAO objects are classified as starburst galaxies, being located more than 0.6 dex above the main-sequence line (Rodighiero et al. 2011). This is consistent with

³⁵ $\log(L_{X, \text{SF}}/1.21) = 39.49 + 0.74 \times \log(9.8 \times 10^{-11} L_{\text{IR}}) L_{\odot}$.

³⁶ <http://lambic.astrosen.unam.mx/cstack/>

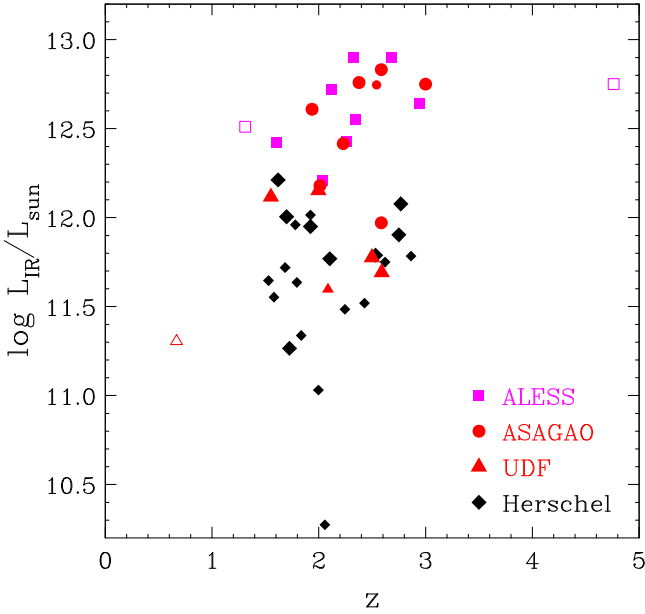


Figure 1. Relation between redshift (z) and infrared luminosity in the rest-frame 8–1000 μm band (L_{IR}) for various samples. Red filled circles: *Chandra*-detected sources in the ASAGAO sample that are classified as AGNs at $z = 1.5$ –3. Red filled triangles: *Chandra*-detected sources in the UDF sample (D17) that are classified as AGNs at $z = 1.5$ –3. Red open triangle: UDF9 (not AGN). Magenta filled squares: the ALESS-AGN sample (Wang et al. 2013) at $z = 1.5$ –3. Magenta open squares: those not at $z = 1.5$ –3. Black diamonds: the *Herschel*-AGN sample ($z = 1.5$ –3). Smaller symbols correspond to objects with stellar masses of $\log M_*/M_\odot < 10.5$.

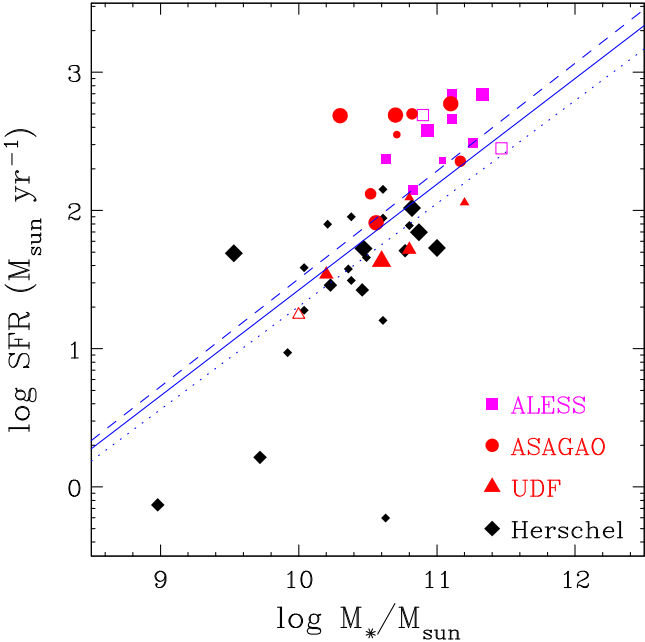


Figure 2. Correlation between stellar mass and star-forming rate (SFR). Red filled circles: *Chandra*-detected sources in the ASAGAO sample that are classified as AGNs at $z = 1.5$ –3. Red filled triangles: *Chandra*-detected sources in the UDF sample (D17) that are classified as AGNs at $z = 1.5$ –3. Red open triangle: UDF9 (not AGN). Magenta filled squares: the ALESS-AGN sample (Wang et al. 2013) at $z = 1.5$ –3. Magenta open squares: those not at $z = 1.5$ –3. Black diamonds: the *Herschel*-AGN sample ($z = 1.5$ –3). Large, medium, and small symbols correspond to objects at $z = 2.5$ –3, $z = 2$ –2.5 and $z = 1.5$ –2, respectively. The blue lines denote the main sequence relations at $z = 2.75$ (dashed), $z = 2.25$ (solid), and $z = 1.75$ (dotted), according to Speagle et al. (2014).

previous ALMA survey results for faint sub/millimeter galaxies (e.g., Hatsukade et al. 2015; Yamaguchi et al. 2016). The AGNs undetected by ALMA generally follow the same correlation at lower stellar-mass or SFR ranges.

4.2. AGN Fraction

We derive the AGN fraction in the millimeter galaxies down to an X-ray flux limit of $\sim 5 \times 10^{-17} \text{ erg cm}^{-2} \text{ s}^{-1}$ (0.5–7 keV), which is 5 times fainter than that of the ALESS-AGN sample (Wang et al. 2013). Following Wang et al. (2013), we calculate the cumulative AGN fraction at $f_X > f_{X,\text{lim}}$ as $\sum_{i=1}^N (1/N_{\text{MG},i})$, where the suffix i (1 through N) represents each *Chandra*-identified AGN with a flux of $f_{X,i}$ ($> f_{X,\text{lim}}$) and $N_{\text{MG},i}$ is the total number of ALMA objects that would be detected if they had fluxes brighter than $f_{X,i}$. We find that the AGN fraction in the ASAGAO sample (with a flux-density limit of $> 0.6 \text{ mJy}$ at 1.2 mm) is $67^{+15}_{-19}\%$ at $f_X > 5 \times 10^{-17} \text{ erg cm}^{-2} \text{ s}^{-1}$ (0.5–7 keV), whereas that in the UDF sample covering a flux-density range of 0.15–0.31 mJy at 1.3 mm (or 0.18–0.39 mJy at 1.2 mm) is $38^{+18}_{-15}\%$ at $f_X > 4 \times 10^{-17} \text{ erg cm}^{-2} \text{ s}^{-1}$ (0.5–8 keV). When we limit the sample to those at $z = 1.5$ –3, we obtain AGN fractions of $88^{+10}_{-24}\%$ in the ASAGAO sample and $63^{+19}_{-24}\%$ in the UDF sample (at the same X-ray flux limits as above).

The best-estimated AGN fraction obtained from the ASAGAO sample is higher than that from the UDF sample, although the significance of the difference is marginal due to the limited sample size. This is most likely related to the lower SFRs (and hence lower IR luminosities) or smaller stellar masses in the latter sample. In fact, when we divide the combined ASAGAO+UDF sample at $z = 1.5$ –3 by IR luminosity, we find AGN fractions of $90^{+8}_{-19}\%$ at $f_X > 5 \times 10^{-17} \text{ erg cm}^{-2} \text{ s}^{-1}$ (0.5–7 keV) for the ULIRGs ($\log L_{\text{IR}} = 12$ –12.8), and $57^{+23}_{-25}\%$ at $f_X > 4 \times 10^{-17} \text{ erg cm}^{-2} \text{ s}^{-1}$ (0.5–8 keV) for the LIRGs ($\log L_{\text{IR}} = 11.5$ –12). The trend is consistent with previous results that the AGN fraction is small among faint millimeter galaxies (Fujimoto et al. 2016) or among $z \sim 2$ galaxies with small stellar masses (Kriek et al. 2007; Yamada et al. 2009; Wang et al. 2017).

Our ASAGAO result ($\sim 90\%$) is even higher than that by Wang et al. (2017), who obtained an AGN fraction of $\sim 50\%$ among their green-color galaxy sample with $\log M_*/M_\odot > 10.6$. This may be related to the fact that the high-resolution observations of ALMA are biased toward more compact objects; if that is the case, these results imply that compact SFGs have remarkably high AGN fractions, as suggested by Chang et al. (2017) for $z < 1.5$ AGNs. On the other hand, the ALESS sources, whose stellar masses are larger than the ASAGAO sample (Figure 1), apparently shows a much smaller AGN fraction ($\sim 20\%$) than ours. A primary reason is its brighter X-ray flux limit, because most of the ALESS region (E-CDFS) is covered only by $\sim 250 \text{ ks}$ exposure of *Chandra*. Indeed, when we impose the same X-ray flux limit as that for the ALESS-AGN sample ($f_X > 2.7 \times 10^{-16} \text{ erg cm}^{-2} \text{ s}^{-1}$), the AGN fraction for the ASAGAO $z = 1.5$ –3 sample becomes $\sim 25\%$, consistent with the ALESS result. Namely, many AGNs in these millimeter galaxies are not X-ray luminous, and hence are only detectable with very deep X-ray data. This trend implies that even $\sim 90\%$ may be a lower limit, becoming higher when the *Chandra* exposure increases beyond 7 Ms.

4.3. X-Ray Absorption Properties

Among the 12 ALMA-*Chandra* sources for which the X-ray hardness ratio is available, 7 have best-fit absorption column

densities of $\log N_{\text{H}}/\text{cm}^{-2} < 22$ (classified as ‘‘X-ray type-1 AGNs’’ according to Ueda et al. 2003) and 5 show $\log N_{\text{H}}/\text{cm}^{-2} \geq 22$ (‘‘X-ray type-2 AGNs’’). While the obscuration fraction (5 out of 12) is consistent with that found from hard (3–24 keV) X-ray-detected U/LIRGs in the COSMOS field at $z = 0.3 - 1.9$ (12 out of 23, Matsuoka & Ueda 2017), it looks much smaller than those of local U/LIRGs; according to a recent study by Ricci et al. (2017), more than 90% of AGNs in late-merger galaxies are subject to heavy obscuration $\log N_{\text{H}}/\text{cm}^{-2} > 23$. Since the X-ray luminosity range of our ALMA-*Chandra* sample is similar to that of typical local U/LIRGs (Section 4.4), the difference cannot be explained by the luminosity dependence of the absorbed AGN fraction (Ueda et al. 2003). In local ULIRGs, star formation activity is concentrated at the nucleus within < 0.5 kpc (Soifer et al. 2000). In contrast, on the basis of JVLA and ALMA imaging, Rujopakarn et al. (2016) reported that main-sequence SFGs at $z \sim 2$ with $\text{SFR} \sim 100 M_{\odot} \text{ yr}^{-1}$ have extended (~ 4 kpc diameter) star-forming regions, whereas the size becomes more compact in more luminous SMGs (see also Chapman et al. 2004; Biggs & Ivison 2008; Ivison et al. 2011 for the results of radio observations). The difference in the host star-forming properties between our ALMA-*Chandra* sample and local ULIRGs would be related to the amount of obscuring gas/dust around the nucleus.

We have to bear in mind, however, that the uncertainty in the column density is often quite large due to the limited photon statistics; a few objects (e.g., ID 1 and UDF7) tentatively classified as unobscured AGNs could even be Compton-thick AGNs ($\log N_{\text{H}}/\text{cm}^{-2} \sim 24$) within the error. In an extreme case, only an unabsorbed scattered component coming from outside the torus may be detected with *Chandra* in heavily Compton-thick AGNs; such objects would be misidentified as (low-luminosity) X-ray type-1 AGNs. In fact, according to a standard population synthesis model of the X-ray background (Ueda et al. 2014), the fraction of Compton-thick AGNs at $f_{\text{X}} \sim 5 \times 10^{-17} \text{ erg cm}^{-2} \text{ s}^{-1}$ (0.5–7 keV) is predicted to be $\sim 20\%$. This corresponds to ~ 3 out of the 14 *Chandra* objects, whereas only one object is identified as Compton-thick based on the best-fit hardness ratio. Nevertheless, considering the small number of possible additional Compton-thick AGNs (~ 2), our main conclusions, discussed below, are not largely affected by this uncertainty, as long as the standard X-ray background model is correct.

4.4. Correlation between Infrared and X-Ray Luminosities

In SFGs containing AGNs, the X-ray and infrared luminosities are good indicators of the mass-accretion rate onto the SMBH (\dot{M}_{BH}) and (dust-embedded) SFR, respectively. Figure 3 plots the relation between the infrared luminosity in the rest-frame 8–1000 μm band (L_{IR}) and the intrinsic X-ray luminosity (L_{X}) for our ALMA-*Chandra* (ASAGAO+UDF) objects. We also plot the *Herschel*-AGN sample, for which L_{IR} is taken from Straatman (2016) and L_{X} is determined from the *Chandra* count rates in the same way as for the ALMA-*Chandra* objects. Furthermore, we plot the ALESS-AGN sample from Wang et al. (2013), the *NuSTAR*-detected U/LIRGs in the COSMOS field from Matsuoka & Ueda (2017), and local ULIRGs for which results from hard X-ray (> 10 keV) observations with *NuSTAR* are published. All the L_{IR} values quoted in Figure 3 are total IR luminosities that include both star-forming and AGN contributions. In the figure, we mark the $L_{\text{X}}-L_{\text{IR}}$ relation expected from

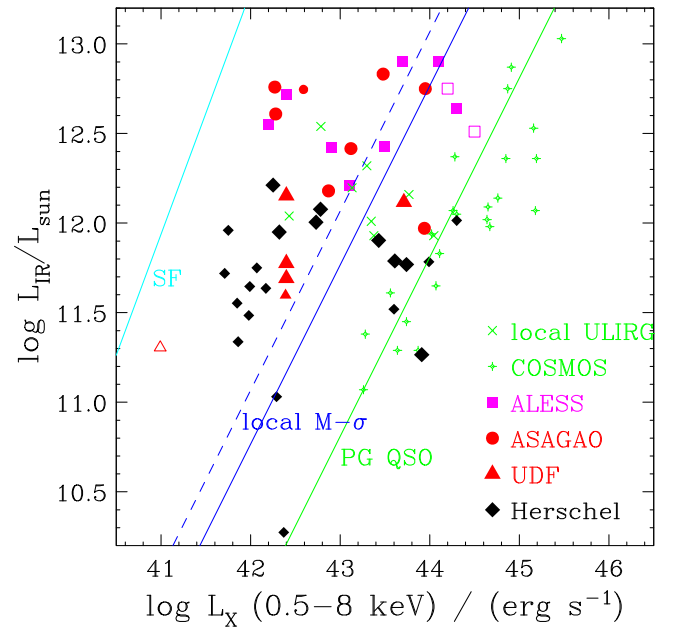


Figure 3. Relation between de-absorbed X-ray luminosity in the rest-frame 0.5–8 keV band (L_{X}) and infrared luminosity in the rest-frame 8–1000 μm band (L_{IR}) for various samples. Red filled circles: *Chandra*-detected sources in the ASAGAO sample that are classified as AGNs at $z = 1.5-3$. Red filled triangles: *Chandra*-detected sources in the UDF sample (D17) that are classified as AGNs at $z = 1.5-3$. Red open triangle: UDF9 (not AGN). Magenta filled squares: the ALESS-AGN sample (Wang et al. 2013) at $z = 1.5-3$. Magenta open squares: those not at $z = 1.5-3$. Black diamonds: the *Herschel*-AGN sample ($z = 1.5-3$). Green diagonal crosses: the *NuSTAR*-detected U/LIRGs in the COSMOS field (Matsuoka & Ueda 2017). Green crosses: local ULIRGs with available *NuSTAR* results (Teng et al. 2015; Oda et al. 2017). Smaller symbols correspond to objects with stellar masses of $\log M_{*}/M_{\odot} < 10.5$. The green solid line represent the mean value for PG QSOs (Teng & Veilleux 2010). The cyan solid line corresponds to a relation for SFGs by Lehmer et al. (2010). The blue solid and dashed lines are the galaxy-SMBH ‘‘simultaneous evolution’’ lines for $A = A_{\text{bul}} (=200)$ (bulge) and $A = A_{\text{tot}} (=400)$ (bulge+disk), respectively.

pure star formation activity, based on the formula by Lehmer et al. (2010) at $\text{SFR} > 0.4 M_{\odot} \text{ yr}^{-1}$. We also mark the relation observed in Palomer–Green (PG) QSOs (i.e., AGN-dominant population, Teng & Veilleux 2010).

We find that our ALMA-*Chandra* AGNs occupy a similar region to local ULIRGs, having a large scatter (> 2 dex) in the $L_{\text{X}}/L_{\text{IR}}$ ratio. Typical statistical errors in L_{X} and L_{IR} that are ≈ 0.2 dex and ≈ 0.1 dex, respectively (Table 1), are much smaller than the scatter. The possible systematic uncertainties in L_{IR} (0.1–0.2 dex, Section 2) also do not affect our conclusions. Figure 4 displays the histogram of $\log L_{\text{X}}/L_{\text{IR}}$ for our ALMA-*Chandra* AGN and that including the *Herschel*-AGN sample. Bimodal distribution is strongly suggested in the latter histogram. More than half of the sources are distributed around a peak centered at $\log L_{\text{X}}/L_{\text{IR}} = -3$, whereas a non-negligible fraction of them show higher $L_{\text{X}}/L_{\text{IR}}$ ratios consistent with AGN-dominant populations. While such a large variation in the $L_{\text{X}}-L_{\text{IR}}$ relation is known in the local universe by combining various samples with different selections (see, e.g., Figure 8 of Alexander et al. 2005), here we find a similar $L_{\text{X}}-L_{\text{IR}}$ variation at $z = 1.5-3$ by directly detecting individual objects on the basis of very deep X-ray and millimeter observations of the common survey field. The mean

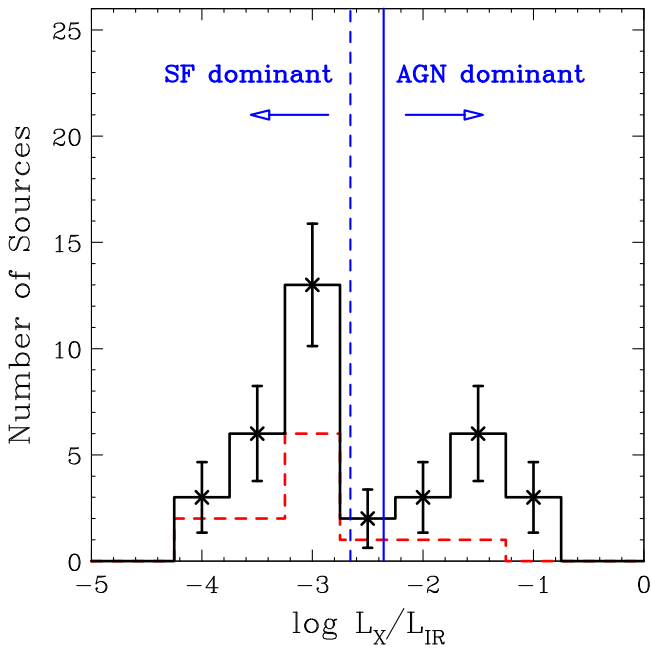


Figure 4. Histograms of $\log L_X/L_{\text{IR}}$ for AGNs in the ASAGAO and UDF samples (red) and for AGNs in the ASAGAO, UDF, and *Herschel*-AGN samples (black). The error bars correspond to the 1σ binomial uncertainties. The blue solid and dashed lines correspond to the galaxy-SMBH “simultaneous evolution” ratios for $A = A_{\text{bul}} (=200)$ (bulge only) and $A = A_{\text{tot}} (=400)$ (bulge +disk), respectively.

IR luminosities for subsamples with $\log L_X = 42\text{--}43$ and $43\text{--}44$ are $\log L_{\text{IR}}/M_\odot = 12.15 \pm 0.08$ and 12.27 ± 0.10 , respectively, which are similar to each other. This is consistent with the result by Stanley et al. (2015) utilizing stacking analysis in which the mean IR luminosities are fairly constant against X-ray luminosity at each redshift. Our result is quite different from previous studies inevitably biased for luminous AGN owing to their bright flux limits (e.g., see Figure 2 of Willott et al. 2013 for optical wide-area surveys, and Matsuoka & Ueda 2017 for a hard X-ray survey with *NuSTAR* in the COSMOS field), whose samples are predominantly located around the PG QSO line in Figure 3. It is interesting to compare our result with the prediction of the co-evolution scenario. We assume the relation (for a Chabrier IMF)

$$\text{SFR} = 1.09 \times 10^{-10} \times L_{\text{IR}}/L_\odot \quad (M_\odot \text{ yr}^{-1}). \quad (1)$$

The X-ray luminosity L_X can be converted to a mass-accretion rate onto the SMBH \dot{M}_{BH} by assuming a radiative efficiency η and a bolometric correction factor $\kappa_{0.5-8}$ as

$$\dot{M}_{\text{BH}} = \kappa_{0.5-8} L_X (1 - \eta) / (\eta c^2), \quad (2)$$

where c is the light speed. Here, we adopt $\eta = 0.05$, as estimated by comparison of the local SMBH mass density and the most updated AGN luminosity function (Ueda et al. 2014).³⁷ By analyzing the combined IR-to-mm SED of their sample, D17 estimated that the averaged fractional AGN contribution to the IR luminosity is $\sim 20\%$. Thus, assuming that 20% of L_{IR} is the intrinsic AGN bolometric luminosity, we can estimate an averaged

³⁷ This estimate of η depends on $\kappa_{0.5-8}$, for which Ueda et al. (2014) assumed luminosity-dependent values by Hopkins et al. (2007). If a constant value of $\kappa_{0.5-8} = 45$ was adopted, we would obtain $\eta \simeq 0.1$. This moves the blue lines in Figures 3 and 4 rightward by 0.3 dex but does not change our conclusions.

bolometric correction factor by comparing with observed X-ray luminosities. Here, we ignore X-ray undetected objects because their intrinsic X-ray luminosities would be highly uncertain if we take into account the possibility of heavily Compton-thick obscuration. Taking a luminosity-weighted average of AGNs in the ASAGAO, UDF, and *Herschel*-AGN samples, we find $\kappa_{0.5-8} \approx 45$ (or $\kappa_{2-10} \approx 70$, a bolometric correction factor from the 2–10 keV luminosity, converted by assuming a photon index of 1.9).

If the galaxy-SMBH evolution is exactly simultaneous over cosmic time, we expect the relation

$$\text{SFR} \times (1 - R) = A \times \dot{M}_{\text{BH}}, \quad (3)$$

where R is the return fraction (the fraction of stellar masses that are ejected back to the interstellar medium; $R = 0.41$ for a Chabrier IMF), and A is the mass ratio of stars to SMBHs in the local universe. Here, we consider two cases: $A = A_{\text{bul}}$ for the stellar masses only in bulge components and $A = A_{\text{tot}}$ for the total stellar masses in both bulges and disks. As a representative value, we use $A_{\text{bul}} \sim 200$, based on the latest calibration by Kormendy & Ho (2013) at a bulge mass of $10^{11} M_\odot$. Adopting a total (bulge+disk) stellar mass density of $\log \rho_*/(M_\odot \text{ Mpc}^{-3}) \simeq 8.6$ (see Madau & Dickinson 2014 and references therein) and a SMBH mass density of $\log \rho_{\text{BH}}/(M_\odot \text{ Mpc}^{-3}) \simeq 6.0$ (Ueda et al. 2014) in the local universe, we estimate $A_{\text{tot}} \sim 400$. From a clustering analysis of $z \sim 2$ galaxies in the COSMOS field, Béthermin et al. (2014) suggested that most of galaxies with $\log M_*/M_\odot \sim 11$ (for a Salpeter IMF) at $z \sim 2$ evolve into bulge-dominated galaxies at $z = 0$, whereas a portion of SFGs with $\log M_*/M_\odot \sim 10$ at $z \sim 2$ become SFGs or passive galaxies with $\log M_*/M_\odot \sim 11$ at $z = 0$. Thus, we expect that the majority of our objects are likely the progenitors of local bulge-dominated galaxies, although a small fraction of them, with $\log M_*/M_\odot \sim 10$, may end up in local disk-galaxies. We therefore adopt $A = A_{\text{bul}}$ as the main assumption in the following discussions.

Combining Equations (1)–(3), we show the “simultaneous evolution” relations in the L_X versus L_{IR} plane by the blue solid (dashed) line in Figures 3 and 4 for the bulge (total) stellar masses. Many objects are not tightly distributed along either of these lines, suggesting that the evolution is not simultaneous in individual galaxies. The “non-coeval” nature is consistent with the finding by Yamada et al. (2009) based on K-band-selected galaxies at $z \sim 2$, although they did not use far-IR/mm data to estimate the SFR. It is seen that the majority of the $z = 1.5\text{--}3$ sources are located above the lines; if our assumptions are correct, stars would be forming more rapidly than SMBHs in these galaxies. There is also a significant fraction of objects located below this line, in which SMBHs are growing more rapidly than the stars.

We note that the bolometric correction factor estimated above, $\kappa_{0.5-8} = 45$, is larger than a nominal value for AGNs with similar X-ray luminosities ($\log L_X \approx 42\text{--}44$), $\kappa_{0.5-8} \approx 5\text{--}20$ (Rigby et al. 2009). Vasudevan & Fabian (2007) showed, however, that the bolometric correction factor sharply correlates with Eddington ratio rather than luminosity: the mean value of κ_{2-10} rapidly increases to ~ 70 (or $\kappa_{0.5-8} \sim 45$) at $\lambda_{\text{Edd}} (\equiv L_{\text{bol}}/L_{\text{Edd}}) \gtrsim 0.1$. This would imply that the Eddington ratios of our AGNs are high, that is, they contain a rapidly growing SMBH with a relatively small black hole mass.

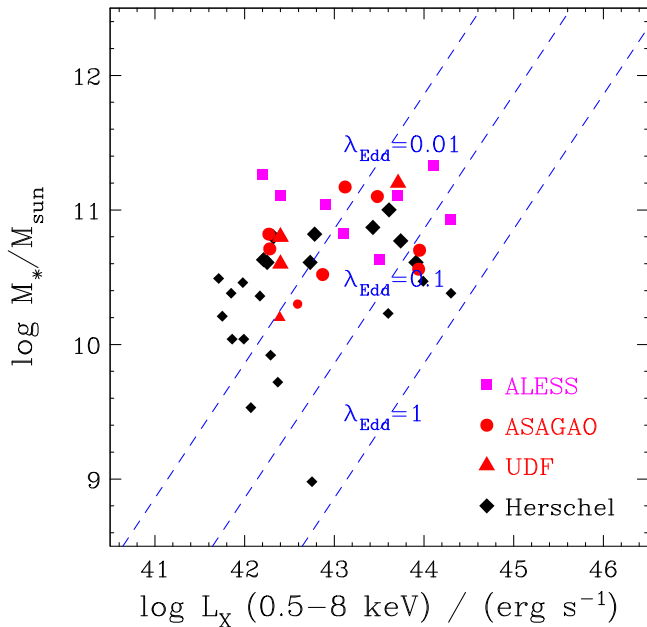


Figure 5. Relation between de-absorbed X-ray luminosity in the rest-frame 0.5–8 keV band (L_X) and stellar mass (M_*). Red filled circles: *Chandra*-detected sources in the ASAGAO sample that are classified as AGNs at $z = 1.5$ –3. Red filled triangles: *Chandra*-detected sources in the UDF sample (D17) that are classified as AGNs at $z = 1.5$ –3. Magenta filled squares: the ALESS-AGN sample (Wang et al. 2013) at $z = 1.5$ –3. Black diamonds: the *Herschel*-AGN sample ($z = 1.5$ –3). Smaller symbols correspond to those with stellar masses of $\log M_*/M_\odot < 10.5$. The dashed lines represent the relations expected for three different Eddington ratios by assuming the local M_* – M_{BH} relation ($A = 200$).

4.5. Correlation between X-Ray Luminosity and Stellar Mass

Figure 5 plots the correlation between X-ray luminosity and total stellar mass for the AGN in the ASAGAO, UDF, *Herschel*-AGN samples. Adopting a bolometric correction factor $\kappa_{0.5-8} = 45$, we plot the relations that would be expected if the ratio of the stellar mass to the black hole mass were $A = 200$ for three assumed values of the Eddington ratio ($\lambda_{\text{Edd}} = 0.01, 0.1$, and 1). Apparently, the majority of the AGNs are located around the $\lambda_{\text{Edd}} = 0.01$ line, indicative of inefficient SMBH accretion. This directly contradicts the previous argument that the SMBHs in our AGN sample have high Eddington ratios ($\lambda_{\text{Edd}} > 0.1$) on average. Time variability in the instantaneous mass-accretion rate (hence in L_X), which could produce a large L_X -to- L_{IR} variation (Hickox et al. 2014), cannot explain this contradiction, as long as we assume the local M_* – M_{BH} relation. This discrepancy can be solved, however, if the black hole mass is ~ 10 times smaller than that expected from the stellar mass with the local M_* – M_{BH} relation, that is, $A \sim 2000$. In Figure 5, we also plot the ALESS-AGN sample at $z = 1.5$ –3; assuming that their Eddington ratios are also high, they would have similarly large A values on average. This implies that these small black hole mass systems may be young galaxies, although we cannot find a clear correlation between the M_*/L_X ratio and the galaxy age derived from the SED fit (available in the ZFOURGE catalog). We leave it to future studies to pursue this issue using a larger sample.

We thus infer that the majority of the ALMA/*Herschel*- and *Chandra*-detected populations, a representative sample of

SFGs with $\log L_{\text{IR}}/L_\odot > 11$ hosting AGNs at $z = 1.5$ –3, are in a star-formation-dominant phase and contain small SMBHs compared to their stellar mass. This picture is in line with earlier suggestions for more luminous (hence rare) SMGs, which are suggested to contain small SMBHs (e.g., Alexander et al. 2005, 2008; Tamura et al. 2010). This may appear to be in contrast to previous reports that luminous AGNs are in an AGN-dominant phase (e.g., Matsuoka & Ueda 2017) and have larger SMBHs than those expected from the local M_* – M_{BH} relation (see Figure 38 of Kormendy & Ho 2013 for a summary). We argue that the apparent contradiction is due to selection bias for luminous AGNs in such studies. In fact, a non-negligible fraction ($\sim 20\%$) of the whole sample, mostly X-ray luminous objects, is located at $\lambda_{\text{Edd}} > 0.1$ lines in Figure 5. They may have SMBHs larger than those expected from the local M_* – M_{BH} relation and truly be accreting with $\lambda_{\text{Edd}} \sim 0.1$.

Recalling that the majority of our sample is likely progenitors of local bulge-dominated galaxies, the star-formation-dominant galaxies with small SMBHs must experience an AGN-dominant phase later, to make the tight M_* – M_{BH} relation at $z = 0$. Indeed, such AGN-dominant, X-ray-luminous populations are present in our sample, and even more luminous AGNs were detected in wider and shallower surveys. Our results are consistent with an evolutionary scenario in which star formation occurs first and an AGN-dominant phase follows later (e.g., Hopkins et al. 2008; Netzer 2009), at least in objects finally evolving into galaxies with classical bulges. If this is the case, the dichotomy in the L_X/L_{IR} distribution (Figure 4) would mean that the transition time from the star formation dominant phase to the AGN-dominant one is short. It is interesting that, despite the wide diversity of populations at $z = 1.5$ –3, the mass-accretion-rate density and the SFR density appear to “co-evolve” by roughly keeping the local M_* – M_{BH} relation (e.g., Mullaney et al. 2012). We suggest that the “co-evolution” view is only valid when the mass-accretion rate and SFR are averaged over a cosmological timescale for an individual galaxy, or when they are averaged for a large number of galaxies in different evolutionary stages at a given epoch.

5. Conclusions

We have reported the first results from our 26 arcmin² ALMA deep survey at 1.2 millimeter on the GOODS-S field (ASAGAO) project, supplemented by the deeper and narrower 1.3 mm survey by D17. This paper focuses on the X-ray AGN properties utilizing the *Chandra* 7 Ms survey data. The main conclusions are summarized as follows:






1. From the ASAGAO survey, we detected 12 mm galaxies with a signal-to-noise ratio of > 5 at a flux limit of ≈ 0.6 mJy, among which 10 are identified by the ZFOURGE catalog. Most of them are luminous ($\log L_{\text{IR}}/L_\odot > 11.5$) main-sequence SFGs at $z = 1.5$ –3.
2. The AGN fraction in the ALMA detected galaxies at $z = 1.5$ –3 is found to be $90_{-19}^{+8}\%$ for the ULIRGs with $\log L_{\text{IR}}/L_\odot = 12$ –12.8 and $57_{-25}^{+23}\%$ for the LIRGs with $\log L_{\text{IR}}/L_\odot = 11.5$ –12. The high AGN fractions among $z = 1.5$ –3 U/LIRGs have been revealed thanks to a much deeper X-ray flux limit ($\approx 5 \times 10^{-17}$ erg cm⁻² s⁻¹




in the 0.5–7 keV band) than those used in previous studies.

- There is a large variation in the L_X/L_{IR} relation in the ALMA- and/or *Herschel*-detected X-ray AGNs at $z = 1.5\text{--}3$. About two-thirds of them have L_X/L_{IR} ratios smaller than the value expected from the local black-hole-mass-to-stellar-mass ($M_{\text{BH}}\text{--}M_*$) relation. This suggests that exactly simultaneous co-evolution does not take place in individual galaxies.
- If the local $M_{\text{BH}}\text{--}M_*$ relation is assumed, the majority of these AGNs apparently show $\lambda_{\text{Edd}} < 0.1$. This contradicts a large bolometric correction factor ($\kappa_{0.5\text{--}8} = 45$) estimated from the IR SED analysis by D17 and the X-ray luminosities. We infer that a large fraction of star-forming galaxies hosting AGNs at $z = 1.5\text{--}3$ have black hole masses smaller than those expected from the local $M_{\text{BH}}\text{--}M_*$ relation. These results are consistent with an evolutionary scenario in which star formation occurs first and an AGN-dominant phase follows later, at least in objects that finally evolve into galaxies with classical bulges.

This paper makes use of the following ALMA data: ADS/JAO.ALMA#2015.1.00098.S. ALMA is a partnership of ESO (representing its member states), NSF (USA) and NINS (Japan), together with NRC (Canada), MOST and ASIAA (Taiwan), and KASI (Republic of Korea), in cooperation with the Republic of Chile. The Joint ALMA Observatory is operated by ESO, AUI/NRAO, and NAOJ. The National Radio Astronomy Observatory is a facility of the National Science Foundation operated under cooperative agreement by Associated Universities, Inc. Part of this work was financially supported by Grants-in-Aid for Scientific Research 17H06130 (Y.U., K.K., and Y.T.) and JP15K17604 (W.R.) from the Ministry of Education, Culture, Sports, Science and Technology (MEXT) of Japan, and by NAOJ ALMA Scientific Research Grant No. 2017-06B. R.J.I. acknowledges support from the European Research Council in the form of the Advanced Investigator Programme, 321302, COSMICISM. T.M. and the development of CSTACK are supported by UNAM-DGAPA PAPIIT IN104216 and CONACyT 252531. W.R. is supported by the Thailand Research Fund/Office of the Higher Education Commission, grant No. MRG6080294.

ORCID iDs

Y. Ueda  <https://orcid.org/0000-0001-7821-6715>
 B. Hatsukade  <https://orcid.org/0000-0001-6469-8725>
 K. Kohno  <https://orcid.org/0000-0002-4052-2394>
 Y. Yamaguchi  <https://orcid.org/0000-0002-7019-4010>
 H. Umehata  <https://orcid.org/0000-0003-1937-0573>
 M. Akiyama  <https://orcid.org/0000-0002-2651-1701>
 Y. Ao  <https://orcid.org/0000-0003-3139-2724>
 I. Aretxaga  <https://orcid.org/0000-0002-6590-3994>
 K. Caputi  <https://orcid.org/0000-0001-8183-1460>
 D. Espada  <https://orcid.org/0000-0002-8726-7685>
 S. Fujimoto  <https://orcid.org/0000-0001-7201-5066>
 M. Imanishi  <https://orcid.org/0000-0001-6186-8792>
 A. K. Inoue  <https://orcid.org/0000-0002-7779-8677>
 R. J. Ivison  <https://orcid.org/0000-0001-5118-1313>
 T. Kodama  <https://orcid.org/0000-0002-2993-1576>
 M. M. Lee  <https://orcid.org/0000-0002-2419-3068>

K. Morokuma-Matsui  <https://orcid.org/0000-0003-3932-0952>
 K. Nakanishi  <https://orcid.org/0000-0002-6939-0372>
 K. Ohta  <https://orcid.org/0000-0003-3844-1517>
 M. Ouchi  <https://orcid.org/0000-0002-1049-6658>
 W. Rujopakarn  <https://orcid.org/0000-0002-0303-499X>
 K. Tadaki  <https://orcid.org/0000-0001-9728-8909>
 I. Tanaka  <https://orcid.org/0000-0002-4937-4738>
 T. Wang  <https://orcid.org/0000-0002-2504-2421>

References

- Aird, J., Coil, A. L., Georgakakis, A., et al. 2015, *MNRAS*, 451, 1892
 Alexander, D. M., Bauer, F. E., Chapman, S. C., et al. 2005, *ApJ*, 632, 736
 Alexander, D. M., Brandt, W. N., Smail, I., et al. 2008, *AJ*, 135, 1968
 Aravena, M., Decarli, R., Walter, F., et al. 2016, *ApJ*, 833, 68
 Béthermin, M., De Breuck, C., Sargent, M., & Daddi, E. 2015, *A&A*, 573, A113
 Béthermin, M., Kilbinger, M., Daddi, E., et al. 2014, *A&A*, 567, A103
 Biggs, A. D., & Ivison, R. J. 2008, *MNRAS*, 385, 893
 Boyle, B. J., & Terlevich, R. J. 1998, *MNRAS*, 293, L49
 Cappelluti, N., Comastri, A., Fontana, A., et al. 2016, *ApJ*, 823, 95
 Chabrier, G. 2003, *PASP*, 115, 763
 Chang, Y.-Y., Le Floch, E., Juneau, S., et al. 2017, *MNRAS*, 466, L103
 Chapman, S. C., Smail, I., Windhorst, R., Muxlow, T., & Ivison, R. J. 2004, *ApJ*, 611, 732
 Clemens, M. S., Negrello, M., De Zotti, G., et al. 2013, *MNRAS*, 433, 695
 da Cunha, E., Charlot, S., & Elbaz, D. 2008, *MNRAS*, 388, 1595
 da Cunha, E., Walter, F., Smail, I. R., et al. 2015, *ApJ*, 806, 110
 Dunlop, J. S., McLure, R. J., Biggs, A. D., et al. 2017, *MNRAS*, 466, 861
 Elbaz, D., Dickinson, M., Hwang, H. S., et al. 2011, *A&A*, 533, A119
 Fujimoto, S., Ouchi, M., Ono, Y., et al. 2016, *ApJS*, 222, 1
 Gaia Collaboration 2016, *A&A*, 595, A2
 Gehrels, N. 1986, *ApJ*, 303, 336
 Hancock, P. J., Murphy, T., Gaensler, B. M., Hopkins, A., & Curran, J. R. 2012, *MNRAS*, 422, 1812
 Hatsukade, B., Ohta, K., Yabe, K., et al. 2015, *ApJ*, 810, 91
 Hickox, R. C., Mullaney, J. R., Alexander, D. M., et al. 2014, *ApJ*, 782, 9
 Hodge, J. A., Karim, A., Smail, I., et al. 2013, *ApJ*, 768, 91
 Hopkins, P. F., Hernquist, L., Cox, T. J., et al. 2006, *ApJS*, 163, 1
 Hopkins, P. F., Hernquist, L., Cox, T. J., & Kereš, D. 2008, *ApJS*, 175, 356
 Hopkins, P. F., Richards, G. T., & Hernquist, L. 2007, *ApJ*, 654, 731
 Ivison, R. J., Papadopoulos, P. P., Smail, I., et al. 2011, *MNRAS*, 412, 1913
 Kawamuro, T., Ueda, Y., Tazaki, F., Ricci, C., & Terashima, Y. 2016, *ApJS*, 225, 14
 Kennicutt, R. C., Jr. 1998, *ARA&A*, 36, 189
 Kirkpatrick, A., Pope, A., Sajina, A., et al. 2015, *ApJ*, 814, 9
 Kormendy, J., & Ho, L. C. 2013, *ARA&A*, 51, 511
 Kriek, M., van Dokkum, P. G., Franx, M., et al. 2007, *ApJ*, 669, 776
 Lehmer, B. D., Alexander, D. M., Bauer, F. E., et al. 2010, *ApJ*, 724, 559
 Luo, B., Brandt, W. N., Xue, Y. Q., et al. 2017, *ApJS*, 228, 2
 Madau, P., & Dickinson, M. 2014, *ARA&A*, 52, 415
 Marconi, A., Risaliti, G., Gilli, R., et al. 2004, *MNRAS*, 351, 169
 Matsuoka, K., & Ueda, Y. 2017, *ApJ*, 838, 128
 McMullin, J. P., Waters, B., Schiebel, D., Young, W., & Golap, K. 2007, in ASP Conf. Ser. 376, *Astronomical Data Analysis Software and Systems XVI*, ed. R. A. Shaw, F. Hill, & D. J. Bell (San Francisco CA: ASP), 127
 Mullaney, J. R., Daddi, E., Béthermin, M., et al. 2012, *ApJL*, 753, L30
 Murphy, E. J., Condon, J. J., Schinnerer, E., et al. 2011, *ApJ*, 737, 67
 Netzer, H. 2009, *MNRAS*, 399, 1907
 Oda, S., Tanimoto, A., Ueda, Y., et al. 2017, *ApJ*, 835, 179
 Ricci, C., Bauer, F. E., Treister, E., et al. 2017, *MNRAS*, 468, 1273
 Rigby, J. R., Diamond-Stanic, A. M., & Aniano, G. 2009, *ApJ*, 700, 1878
 Rodighiero, G., Daddi, E., Baronchelli, I., et al. 2011, *ApJL*, 739, L40
 Rujopakarn, W., Dunlop, J. S., Rieke, G. H., et al. 2016, *ApJ*, 833, 12
 Smail, I., Ivison, R. J., & Blain, A. W. 1997, *ApJL*, 490, L5
 Soifer, B. T., Neugebauer, G., Matthews, K., et al. 2000, *AJ*, 119, 509
 Speagle, J. S., Steinhardt, C. L., Capak, P. L., & Silverman, J. D. 2014, *ApJS*, 214, 15
 Stanley, F., Harrison, C. M., Alexander, D. M., et al. 2015, *MNRAS*, 453, 591
 Straatman, C. M. S., Spitler, L. R., Quadri, R. F., et al. 2016, *ApJ*, 830, 51
 Tamura, Y., Iono, D., Wilner, D. J., et al. 2010, *ApJ*, 724, 127
 Teng, S. H., Rigby, J. R., Stern, D., et al. 2015, *ApJ*, 814, 56

- Teng, S. H., & Veilleux, S. 2010, *ApJ*, 725, 1848
- Ueda, Y. 2015, *PJAB*, 91, 175
- Ueda, Y., Akiyama, M., Hasinger, G., Miyaji, T., & Watson, M. G. 2014, *ApJ*, 786, 104
- Ueda, Y., Akiyama, M., Ohta, K., & Miyaji, T. 2003, *ApJ*, 598, 886
- Vasudevan, R. V., & Fabian, A. C. 2007, *MNRAS*, 381, 1235
- Wang, S. X., Brandt, W. N., Luo, B., et al. 2013, *ApJ*, 778, 179
- Wang, T., Elvaz, D., Alexander, D. M., et al. 2017, *A&A*, 601, A63
- Williams, C., Giavalisco, M., Bezanson, R., et al. 2017, *ApJ*, 838, 94
- Willott, C. J., Omont, A., & Bergeron, J. 2013, *ApJ*, 770, 13
- Wuyts, S., Labbé, I., Förster, S., et al. 2008, *ApJ*, 682, 985
- Xue, Y. Q., Luo, B., Brandt, W. N., et al. 2011, *ApJS*, 195, 10
- Yamada, T., Kajisawa, M., Akiyama, M., et al. 2009, *ApJ*, 699, 1354
- Yamaguchi, Y., Tamura, Y., Kohno, K., et al. 2016, *PASJ*, 68, 82